The effect of confinement and wall structure on the kinetics of isomerisation of *n*-butane

Sarah J. Brookes[a]; Debra J. Searles[a]; Karl P. Travis[b]

[a] Nanoscale Science and Technology Centre and School of Biomolecular and Physical Sciences, Griffith University, Brisbane, Australia [b] Immobilisation Science Laboratory, Department of Engineering Materials, University of Sheffield, Sheffield, UK

First published on: 21 September 2010

PLEASE SCROLL DOWN FOR ARTICLE

The effect of confinement and wall structure on the kinetics of isomerisation of *n*-butane

Sarah J. Brookes[a1], Debra J. Searles[a]* and Karl P. Travis[b2]

[a]*Nanoscale Science and Technology Centre and School of Biomolecular and Physical Sciences, Griffith University, Brisbane, Australia;*
[b]*Immobilisation Science Laboratory, Department of Engineering Materials, University of Sheffield, Sheffield, UK*

We examined the effect of confinement on the torsional kinetics in *n*-butane by conducting equilibrium molecular dynamics (EMD) simulations of the adsorbed phase in a slit-pore geometry. Torsional rate constants were obtained with high precision using the powerful relaxation function method devised by Brown and Clarke (*A direct method of studying reaction rates by EMD: application to the kinetics of isomerization in liquid* n*-butane*, J. Chem. Phys. 92 (1990), pp. 3062–3073). Values of k_{GT}, k_{TG} and k_{GG} were determined as a function of temperature, density and porewidth for two different slit pore models: one employing explicit moving atoms, the other employing a smooth potential, both models being simulated at two different wall surface densities. We observed that direct *gauche–gauche* transitions taking place via the *trans* well (i.e. double well jumps) are significant under all conditions. All rate constants show a linear variation with temperature when plotted in Arrhenius form but the pre-exponential factor has very different density dependence for the double well kinetics compared with the single well transitions (monotone decreasing and monotone increasing, respectively, in the bulk fluid). We also find clear differences between behaviour of the kinetics under confinement compared with the bulk condensed phase results; k_{GG} being generally greater under confinement than for the corresponding bulk systems.

Keywords: confined systems; simulation of rate constants; butane isomerisation

1. Introduction

The molecule *n*-butane (C_4H_{10}) is the simplest example of a hydrocarbon that exhibits the characteristic torsional flexibility typical of most large aliphatic hydrocarbons. Its torsional isomerisation has first order kinetics, and therefore provides a natural starting point for modelling the kinetics of conformational change of more complex molecules, as well as being of pedagogical interest. Understanding the degree to which confinement can affect reaction rates and reaction pathways is likewise of theoretical interest but is also of significance in industrial processes involving heterogeneous catalysis. Butane isomerisation kinetics has thus been the subject of numerous computational investigations under a range of conditions in the bulk fluid, solutions [1–5], and more recently, by our group for confined dense fluids [6], and by Santiso et al. [7] for highly confined, dilute fluids.

Experimental and computational studies have been carried out on the structure of chain molecules near surfaces and under confinement (for some examples see [8–15], and references therein). In a number of experiments unbranched alkanes have been observed to preferentially lie flat and parallel to the surfaces, and scanning tunnelling microscopy experiments of alkanes and haloalkanes on graphite show them adopting a *trans* conformation with the molecule lying flat on the graphite surface [16–18]. This behaviour is reproduced in molecular dynamics simulations. Studies on confined alkanes show layering and ordering of chains under high confinement (see [19] and references therein). Our recent studies on dense butane confined in slit-like pores have also demonstrated that the kinetics of isomerisation of *n*-butane is affected by confinement. Despite the extensive interest and research in this area, there are many questions to resolve regarding the structure, dynamics and kinetics of confined liquids at equilibrium and away from equilibrium [20].

In our recent work [6], we examined the effect of confinement on the *trans–gauche* and *gauche–trans* kinetics for a range of conditions, and showed that at a density of $8.28 \, \text{nm}^{-3}$, the position of the *trans–gauche* equilibrium is displaced towards excess *trans* compared with the bulk phase, reflecting the confinement and interactions of the molecules with the pore wall. The values of the rate constants describing the conversion of *gauche* conformers to the *trans* form and vice versa, (k_{GT} and k_{TG}, respectively) were found to decrease with decreasing pore width. Furthermore, it was observed that the kinetics obeyed an Arrhenius rate law: $k = A \text{e}^{-E_a/(RT)}$ where A is the collision frequency, E_a is the activation energy, T is the temperature and R is the universal gas constant; with E_a for the *trans–gauche* and *gauche–trans* interconversions slightly reduced compared to their values for a bulk fluid at the same density.

*Corresponding author. Email: d.bernhardt@griffith.edu.au

In this article, we extend our investigation into the effects of confinement and state point dependence on the rate of isomerisation of *n*-butane. In particular we examine the kinetics of direct *gauche–gauche* transitions that take place via the *trans* well and investigate the effect of changing the physical properties of the pore walls, including wall flexibility and smoothness, as they have been shown to be very important in past studies [21–24].

Our paper is organised as follows: we begin by discussing the macroscopic rate laws and mechanism postulated to occur in the (bulk) condensed phase. We then briefly discuss the method used to determine the rate constants via the relaxation function method of Brown and Clarke [2]. The model and simulation details are then presented including details of the confined systems and different pore wall models employed. Results are then given and discussed before conclusions are drawn.

2. Macroscopic rate laws

Motion about the central C—C bond in *n*-butane is restricted by a torsional potential. This potential, which is a periodic function of the dihedral angle, α, possesses three minima which correspond to the configurations in which the opposing methyl groups are as far apart as possible (lowest energy conformational state or *trans*-form) or are in the closest proximity to one another without inducing any torsional strain (*gauche*-form). At finite temperature, the presence of these minima gives rise to three distinct conformational states of *n*-butane. Conversion from one of these states to another is an activated process, involving the crossing of a potential energy barrier. Figure 1, which shows a typical torsional potential used in simulations of *n*-butane, illustrates the three minima and energy barriers described above. The maxima in the torsional potential surface provide a partition on the torsional angle space, defined as the semi-open interval
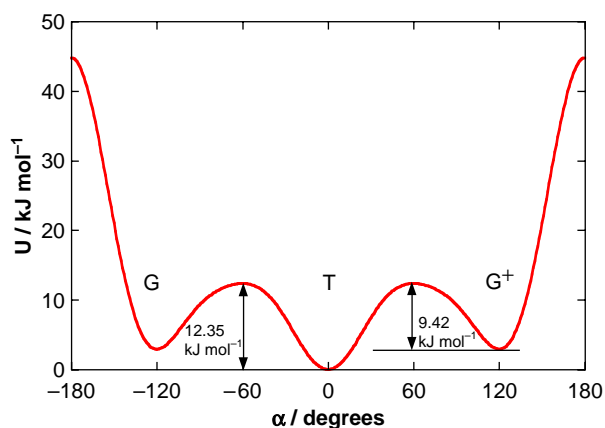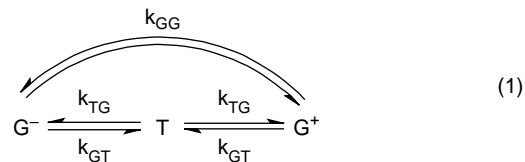

Figure 1. The Ryckaert–Bellemans torsional potential for *n*-butane.

[−180,180), into three subsets: *gauche* $^{-}$, $G^{-} \equiv \psi_1 = \{\alpha: -180 \leq \alpha \leq -60\}$; *trans*, $T \equiv \psi_2 = \{\alpha: -60 < \alpha < 60\}$; and *gauche* $^{+}$, $G^{+} \equiv \psi_3 = \{\alpha: 60 \leq \alpha < 180\}$. A state of dynamic equilibrium exists between these three conformational states. The mechanisms involved can be depicted using the following diagram:

$$
\begin{array}{c}
\overset{\textstyle k_{GG}}{\overgroup{\qquad\qquad\qquad}} \\
G^{-} \underset{k_{GT}}{\overset{k_{TG}}{\rightleftharpoons}} T \underset{k_{GT}}{\overset{k_{TG}}{\rightleftharpoons}} G^{+}
\end{array}
\qquad (1)
$$

where the labels refer to rate constants describing the conversion of one conformational state into another. This mechanism allows for direct *gauche–gauche* transitions. These may occur in either of two ways: by crossing of the *gauche–gauche* energy barrier or through a double well crossing via the *trans* state. The former is unlikely to be observed except at very high temperature. Double-jumps on the other hand, are a well-known mechanism in many processes such as the diffusion of adsorbed atoms [25] and protein unfolding (see, for example [26]). Brown and Clarke [2,3] have already demonstrated that interconversion between the two *G* conformers can be significant in the isomerisation of *n*-butane. They observed a significant number of double-jumps from one *G* well to the other involving traversal of both the *G–T* and *T–G* barriers, without the molecule settling into a *T* conformation. However, no crossings of the much higher *G–G* barrier were observed in any of their simulations. Only when these double crossings are taken into account do the simulation results agree with the predictions of macroscopic kinetics.

The macroscopic rate equations (assuming first order kinetics) describing the rate of production of each fraction of conformer, can be written compactly as

$$\dot{X}_T = -2k_{TG}X_T + k_{GT}(X_{G^-} + X_{G^+}), \qquad (2)$$

$$\dot{X}_{G^+} = k_{TG}X_T - k_{GT}X_{G^+} + k_{GG}X_{G^-} - k_{GG}X_{G^+}, \qquad (3)$$

$$\dot{X}_{G^-} = k_{TG}X_T - k_{GT}X_{G^-} + k_{GG}X_{G^+} - k_{GG}X_{G^-}, \qquad (4)$$

where the dot overstrike signifies a time derivative and the time arguments (on the mole fractions) have been suppressed for the sake of brevity. The variables, X_{G^-} and X_{G^+} can be eliminated from Equation (2) through use of the constraint relation,

$$X_T + X_{G^-} + X_{G^+} = 1, \qquad (5)$$

yielding,

$$\dot{X}_T = -kX_T + k_{GT}, \qquad (6)$$

where the constant, $k = 2k_{TG} + k_{GT}$. Equation (6) is now decoupled from Equations (3) and (4), and thus can

be solved independently of them (using an integrating factor of e^{kt}, for example). The solution is:

$$X_T(t) = X_T(0)e^{-kt} + \frac{k_{GT}}{k}(1 - e^{-kt}). \qquad (7)$$

Equations (3) and (4) may also be solved independently of each other by substitution of Equation (7) and the constraint relation, Equation (5), followed by multiplication with an integrating factor to yield exact differentials. In the case of X_{G^-}, the integrating factor is $e^{\lambda t}$ where λ is a new composite constant term defined by $\lambda = k_{GT} + 2k_{GG}$. The solution is:

$$X_{G^-}(t) = \frac{1}{2}\left[\frac{k_{GT}}{k} - X_T(0)\right](e^{-kt} - e^{-\lambda t}) \\ + X_{G^-}(0)e^{-\lambda t} + \frac{k_{TG}}{k}(1 - e^{-\lambda t}). \qquad (8)$$

The solution for X_{G^+} follows trivially from the constraint relation. The equilibrium conformer fractions: $\bar{X}_T$, $\bar{X}_{G^-}$ and $\bar{X}_{G^+}$ may be obtained from the steady state solutions of Equations (2)–(4), or alternatively, by taking the limit $t \to \infty$ in the integrated rate equations, giving: $\bar{X}_T = k_{GT}/k$, $\bar{X}_{G^-} = \bar{X}_{G^+} = k_{TG}/k$.

3.   Determination of rate constants

To determine the rate constants, we use the relaxation function approach developed by Brown and Clarke [2,3]. The power of this method lies in the fact that it is an equilibrium method, and does not involve perturbing the system in any way. Essentially one identifies a subset of molecules from an equilibrium distribution that are in a particular conformational state. The number of molecules from this original subset that either remain in this state, or are converted to another state is then monitored as a function of time. A relaxation function can be defined which then allows one to estimate the relevant rate constants.

The Brown and Clarke relaxation function is an autocorrelation function of the conformational characteristic function, $H: [-180, 180) \to \{0, 1\}$, defined by

$$H_{\psi_k}(\alpha) = \begin{cases} 1 & \text{if } \alpha \in \psi_k \\ 0 & \text{if } \alpha \notin \psi_k \end{cases} \qquad (9)$$

A family of these relaxation functions can be defined in a compact way through

$$R_{\psi_k,\psi_l}(t) = \langle H_{\psi_k}(\alpha_i(0))H_{\psi_l}(\alpha(t))\rangle, \qquad (10)$$

where the angled brackets denote an average over a set of time origins and the index i implies an additional averaging over molecules (equivalently, torsional angles, α_i). Since $R_{\psi_k,\psi_l}(t)$ refers to the number of molecules

originally in state ψ_k that are in state ψ_l at time t_0, it is directly related to $X_{\psi_l}(t)$ evaluated with $X_{\psi_k}(0) = 1$ (and $X_{\psi_l \neq \psi_k}(0) = 0$). That is, $X_{\psi_l}(t)_{X_{\psi_k}(0)=1} = (R_{\psi_k,\psi_l}(t))/\bar{X}_{\psi_k}$. Therefore for any, ψ_k ψ_l the relaxation functions can be written in terms of the rate constants. Below the notation is simplified by noting $\psi_1 \equiv G^-$, $\psi_2 \equiv T$ and $\psi_3 \equiv G^+$. In order to determine k, a normalised form of $R_{TT}(t)$ was considered,

$$\frac{R_{T,T}(t) - \bar{X}_T^2}{\bar{X}_T - \bar{X}_T^2} = \frac{X_T(t)_{X_T(0)=1} - \bar{X}_T}{1 - \bar{X}_T} = e^{-kt}, \qquad (11)$$

and k was determined by linear regression. The values of k_{TG} and k_{GT} can be obtained using $\bar{X}_T = k_{GT}/k$ and $k = 2k_{TG} + k_{GT}$, as introduced above. The value of k, was then substituted into the relaxation functions for the *gauche* conformers,

$$\frac{R_{G^\pm,G^\pm}(t)}{\bar{X}_{G^\pm}} = X_{G^\pm}(t)_{X_{G^\pm}=1} \\ = \frac{1}{2}\bar{X}_T(e^{-kt} + e^{-\lambda t}) + \bar{X}_{G^\pm}(1 - e^{-\lambda t}) + e^{-\lambda t}, \qquad (12)$$

$$\frac{R_{G^\pm,G^\pm}(t)}{\bar{X}_{G^m}} = X_{G^\pm}(t)_{X_{G^\pm}=1} \\ = \frac{1}{2}\bar{X}_T(e^{-kt} - e^{-\lambda t}) - \bar{X}_{G^\pm}(1 - e^{-\lambda t}) \qquad (13)$$

and non-linear least squares fits to the numerical data gave the value of λ. Finally, the relationship $\lambda = k_{GT} + 2k_{GG}$ was used to obtain k_{GG}.

In most cases, we are interested in calculating the global rate constant for the whole system. However, in the confined systems where the density profile and the distribution of the molecules between the conformers varied with distance from the wall, it is also interesting to consider if there is a variation of the rate constant across the pore. Since the fluid readily diffuses in this direction normal to the pore, there is some arbitrariness in determining how this is calculated. Indeed the relaxation times were typically monitored for periods much longer than the time it would take a molecule to diffuse across the pore. A number of options were considered, but the most reasonable approach was, at any time, t, to only consider contributions to the relaxation function from molecules that were currently in the bin of interest. That is, for any bin n,

$$R_{\psi_k,\psi_l,n}(t) = \frac{\langle N_{\psi_k,\psi_l}(t_0, t_0 + t)\rangle}{N} \\ = \langle H_{\psi_k}[\alpha_i(0)]H_{\psi_l}[\alpha_i(t)]S_n(z_i(t))\rangle, \qquad (14)$$

where $S_n(z_i(t))$ is unity when the molecule is situated in bin n and $S_n(z_i(t))$ is zero when the molecule is not in bin n. The other relations above still hold using this localised

relaxation function, the averages referring to the local averages.

4. Simulations

We have conducted a series of equilibrium molecular dynamics simulations of *n*-butane both in the bulk phase and for an adsorbed phase in which the butane molecules are sandwiched between two parallel walls (slit pore model). Our main interest in this article is the effect of confinement on isomerisation kinetics. The bulk phase simulations were conducted for the purpose of extending our earlier published work to include a full study of the state point dependence of the rate constant describing direct *gauche–gauche* transitions (via the *trans* well), as well as providing a reference state to which the confined simulations could be compared.

The model used for *n*-butane is the same as the one introduced by Ryckaert and Bellemans [27] (RB) in 1978, which is a 4-site Lennard-Jones model incorporating a realistic torsional potential to provide internal flexibility (see Figure 1). Each of the CH_3 or CH_2 groups are treated as identical, united atoms. Although more realistic models now exist, we choose to use this potential so that comparison with earlier results can be made. The model is described in detail in [6]. Bond-lengths and bond-angles were constrained using Lagrange multipliers and numerical error was corrected for using integral feedback. Intermolecular interactions between sites on different molecules of butane were modelled using a spherically truncated Lennard-Jones potential with a cut off radius of 2.5 σ. Each butane site has the same value of the Lennard-Jones parameters σ and ε: $\sigma = 0.3923$ nm, $\varepsilon/k_B = 72$ K, and a mass of 2.411×10^{-26} kg.

Two different slit-pore models were studied in this work. The first model employed fully explicit atomic walls while the second model employed a smooth potential to represent the walls. The explicit atom model was used for comparison with our earlier work on the effects of confinement on butane isomerisation [6]. This model, introduced by Powles et al. [28] consists of parallel layers of vibrating atoms (with Hooke's law restoring forces). The main features being the porous nature of the wall resulting from a low surface density, and the existence of lattice phonons, which enable the walls to act as heat reservoirs or thermostats. In practice the degree of porosity can be controlled in this model by making the harmonic restoring forces stiffer. In our simulations, we employed walls comprising of three layers of atoms placed parallel to each other and to the *xy* plane. The 'atoms' are in fact united atom centres having the same mass and interaction parameters as the sites in *n*-butane molecules. Interplane spacing was taken to be σ. Atoms within each layer were arranged in an fcc lattice consistent with either of two surface densities: 3.25 nm^{-2}, as used in our earlier work

[6], and 3.9 nm^{-2} to examine the effects of an increase in wall density. A slit pore is created by employing periodic boundary conditions in all Cartesian directions, which means that only one 3-layer-thick wall is required per simulation cell. Wall atoms interacted both with each other (necessary for production of phonons), and with sites on fluid molecules. To prevent the fluid from pushing the walls apart a set of holonomic constraints were employed to keep the centre of mass of each layer fixed at its time zero value. More details on how to implement the Powles slit-pore model may be found in [6].

The physical pore width is defined to be the distance between the centre-of-masses of the two wall layers that are in contact with the fluid. Here we consider (physical) pore widths of 4σ, 6σ, 8σ and 10σ, with some additional calculations carried out with a pore width of 30σ to examine the convergence to the bulk limit.

Our second wall model used a Steele 10-4-3 potential in place of the explicit wall atoms [29]. The use of this potential alongside the Powles model allowed us to explore the effects of wall smoothness, wall flexibility and walls which have a much greater surface density typical of those found in covalently bonded solids. These factors have been shown to be very important in past studies [21–24]. The Steele 10-4-3 potential is obtained by averaging the effects of layers of graphene sheets, and only varies in the direction perpendicular to the wall, and is therefore smooth. It is also impermeable. We select a surface density that matches earlier work, and then also consider a surface density corresponding to graphene. The potential due to a single wall is given by:

$$U(z) = 2\pi\varepsilon\sigma^2\rho\Delta\left[\frac{2}{5}\left(\frac{\sigma}{z}\right)^{10} - \left(\frac{\sigma}{z}\right)^4 - \frac{\sigma^4}{3\Delta(z + 0.61\Delta)^3}\right],$$
(15)

where z is the distance of the fluid site from the wall, and the force on a fluid site is given by the sum of the interaction of the two walls. We use parameters typical of graphite: $\sigma = 0.340$ nm, $\varepsilon = 28$ K, and $\Delta = 0.335$, however as well as a particle density of $\rho = 114$ nm^{-3} (which corresponds to graphite), we also consider $\rho = 9.7$ nm^{-3} which then gives a surface density of 3.25 nm^{-2}, matching that of the atomically structured walls considered above. Specular boundary conditions were employed in all simulations involving Steele potential walls.

The simulation algorithm used here is the same as that described in our earlier work, [6] with a 5th order Gear algorithm used to integrate the equations of motion and a timestep of $t^* = t \times (1/\sigma)\sqrt{\varepsilon/M} = 0.0005$, which is approximately 2 fs in real time units. For the bulk simulations and simulations with Steele 10-4-3 walls, a Gaussian thermostat was employed to fix the translational temperature to the desired value. For simulations where

the fluid was confined between atomic walls, the same thermostat was applied to the moving wall atoms to maintain a constant *wall* kinetic temperature. Temperatures between 150 and 500 K were considered with fluid number densities of $\rho = 6.05$, 7 and 8.28 nm^{-3} examined in bulk and confined studies with some additional simulations at $\rho = 9.28$ nm^{-3} for the confined system. Note that we have chosen to define the density of the pore fluid in this work to be $\rho = N/(L_x \times L_y \times W)$, where $W = H - \sigma$, where H is the physical pore width (i.e. the distance between the fixed centre of mass of the wall layers that are in contact with the fluid in the case of the atomic fluids). As we discuss below, there is no 'real' pore width in the case where the wall atoms move. Therefore, although the density above is well defined and a good estimate of the average physical density, one should be aware of its limitations in this case. The bulk simulations and those of fluids confined between atomically structured walls were periodic in all three dimensions. The fluids confined between the Steele 10-4-3 walls were periodic in directions parallel to the wall. This wall is fixed and the interaction potential with fluid molecules diverges to infinity, and therefore it is unnecessary to consider periodicity in the direction normal to the wall. The bulk simulations comprised of 500 molecules whereas the confined systems typically used between 368 and 504 molecules depending on the pore width used, and with 1450 molecules for the pore of width 30σ.

Bulk simulations were conducted for a total of two million timesteps while confined simulations were each conducted for a total of 20 million (production) simulation steps (following equilibration runs of $1-2$ million steps). Equipartition of thermal energy between the wall and fluid was taken as a guide to the existence of an equilibrium state.

5. Results

Prior to calculating the various rate constants, we first checked that the relaxation function data was consistent with the integrated macroscopic rate equations. We found good agreement between simulation and macroscopic kinetics for all simulations, bulk and confined, confirming the 1st order nature of the isomerisation process.

Initially, we examined the kinetics of *n*-butane isomerisation in bulk systems at various state points. The various rate constants were then obtained from fits of Equations (11)–(13) to the relaxation function data. Figure 2 shows the typical behaviour of $R_{G^+,G^+}(t)/\bar{X}_{G^+}$ and $R_{G^+,G^-}(t)/\bar{X}_{G^+}$ obtained for two bulk systems with $\rho = 6.05$ nm^{-3}, and temperatures of 291.6 and 500 K. It is evident from this figure that the results are consistent with the assumed mechanism shown in (1); if the mechanism did not account for the possibility of transitions from one G well to another, $R_{G^+,G^-}(t)/\bar{X}_{G^+}$ would have a vanishing
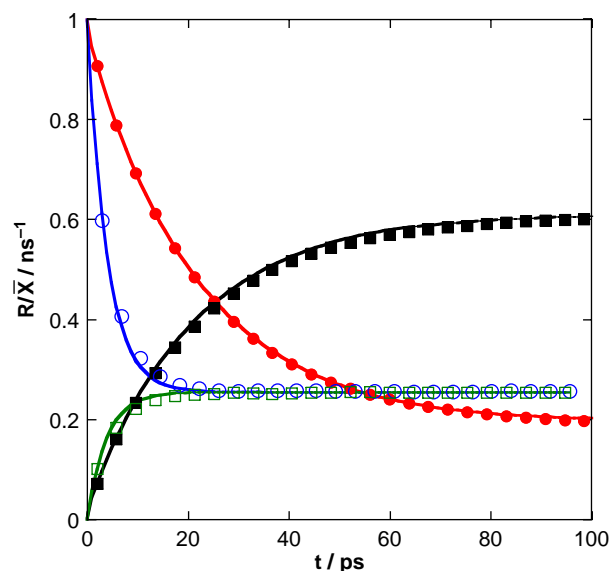

Figure 2.   The relaxation curves $R_{G^+,G^+}(t)/\bar{X}_{G^+}$ (circles) and $R_{G^+,G^-}(t)/\bar{X}_{G^+}$ (squares). For clarity, only every 4th data point is shown. All data is for a bulk system with a density of $\rho = 6.05$ nm^{-3}. The filled symbols are data obtained at a temperature of 291.6 K and the empty symbols at 500 K. The full lines are obtained from the nonlinear fit of the data to the relaxation curves (12) and (13).

tangent near the origin as noted by Brown and Clarke [2]. By examining the variation of torsional angles as a function of time we determined that no transitions occurred across the $G–G$ barrier under any of the conditions that we considered. However, an appreciable number of transitions from $G^{\pm}$ to $G^{\mp}$ through the T well were observed.

Rate constants were obtained for all state conditions examined. The values of k_{GT} and k_{GG} are collected in Table 1 (results for k_{TG} can be found in [6]). As a verification of our present computer codes and analysis tools, it is instructive to compare our k_{GG} data with that in [2]. Brown and Clarke calculated k_{GG} at only one state point, namely a temperature of 291.6 K and density of 6.05 nm^{-3}, obtaining a value of 9.2 ± 0.6 ns^{-1}. This is in agreement with the value from our work of $k_{GG} = 8.9 \pm 0.2$ ns^{-1} for the same set of conditions.

The state point dependence of the rate constants follows several trends. All rate constants are monotonically increasing functions of temperature. As shown in Figure 3, when these data are plotted in Arrhenius form, the transformed points are linear across the whole temperature range, reflecting the activated nature of the isomerisation process. The ratio of k_{GT} to k_{GG} decreases significantly with increasing temperature (e.g. for $\rho = 6.05$ nm^{-3}, $k_{GT}/k_{GG} = 8.2$ at 150 K and $k_{GT}/k_{GG} = 2.1$ at 500 K), signifying that at higher temperatures a larger percentage of molecules have enough energy to go

Table 1. The rate constants k_{GT}, k_{GG} and their ratio for bulk butane at the three number densities (ρ) at various temperatures (T).

T (K)	k_{GT} (ns^{-1})			k_{GG} (ns^{-1})			k_{GT}/k_{GG}		
	$\rho = 6.05\,\text{nm}^{-3}$	$\rho = 7\,\text{nm}^{-3}$	$\rho = 8.28\,\text{nm}^{-3}$	$\rho = 6.05\,\text{nm}^{-3}$	$\rho = 7\,\text{nm}^{-3}$	$\rho = 8.28\,\text{nm}^{-3}$	$\rho = 6.05\,\text{nm}^{-3}$	$\rho = 7\,\text{nm}^{-3}$	$\rho = 8.28\,\text{nm}^{-3}$
150	1.24(2)	1.35(2)	1.31(1)	0.15(2)	0.14(2)	0.04(1)	8.2	9.9	33.8
200	5.98(3)	7.44(2)	7.89(3)	1.21(6)	1.15(3)	0.39(4)	4.9	6.7	20.2
250	16.22(8)	20.58(8)	23.06(6)	4.2(1)	3.99(8)	1.71(7)	3.8	5.2	13.4
291.6	28.7(1)	36.9(1)	43.4(1)	8.9(2)	8.4(1)	4.2(1)	3.2	4.4	10.0
350	52.5(1)	67.7(2)	78.9(2)	19.3(3)	18.4(2)	9.8(2)	2.7	3.7	8.1
400	78.7(1)	101.7(2)	117.8(2)	31.1(4)	29.3(3)	15.1(2)	2.5	3.5	7.3
450	104.2(3)	137.2(3)	161.0(4)	48.5(9)	44.3(5)	25.1(3)	2.1	3.1	6.4
500	138.6(3)	176.6(4)	206.6(8)	66(1)	61.9(8)	35.5(4)	2.1	2.9	5.8

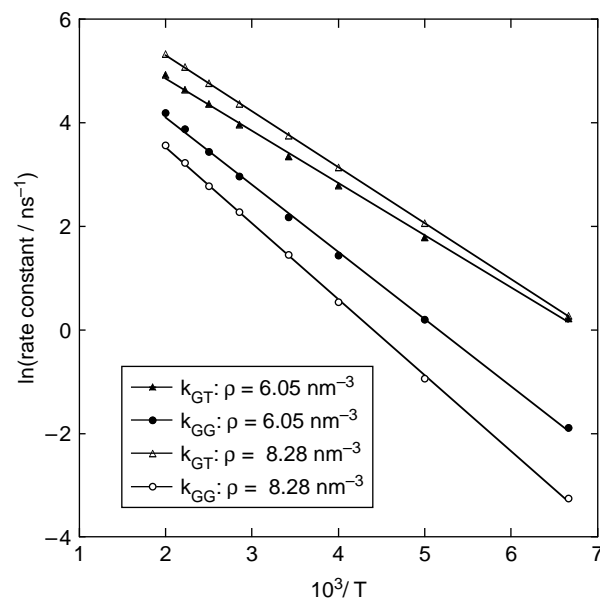The numbers in parentheses give the standard error in the last figure.

Figure 3. Arrhenius plots of k_{GT} (triangles) and k_{GG} (circles) for bulk butane at two densities: $\rho = 6.05\,\text{nm}^{-3}$ (filled symbols) $\rho = 8.28\,\text{nm}^{-3}$ (open symbols).

directly from a $G^{\pm}$ to a $G^{\mp}$ configuration. Also interesting is the behaviour of the rate constants with density at fixed temperature. Here we observed opposite trends for k_{GT} and k_{GG}. With the exception of the lowest temperature data, the former is monotone increasing with density while the latter is monotone decreasing. In the case of k_{GT} we noted previously that the kinetics showed Arrhenius behaviour, and using the data in Figure 3 the activation energies for the *gauche–trans* isomerisation are determined to be 8.4 ± 0.1 and $9.00 \pm 0.03\,\text{kJ}\,\text{mol}^{-1}$ at $\rho = 6.05$ and $8.28\,\text{nm}^{-3}$, respectively. These values are very similar to those calculated in [6], with the discrepancies resulting from slight differences in the low temperature values of k_{GT}. A similar treatment of the current results for k_{TG} gives activation energies for the *trans–gauche* transition of 11.5 ± 0.1 and $11.74 \pm 0.02\,\text{kJ}\,\text{mol}^{-1}$ at $\rho = 6.05$ and $8.28\,\text{nm}^{-3}$, respectively. As discussed previously [6], these reflect a lowering of the effective energy barriers due to solvation. In these cases, the pre-exponential factor in the Arrhenius rate law can be interpreted as a collision frequency. Therefore an increase in density can be expected to give rise to an increase in this factor, explaining the observed trend: the pre-exponential factor for an Arrhenius fit to k_{GT}, increases from 960 ± 50 to $1770 \pm 20\,\text{ns}^{-1}$ as the density is increased from $\rho = 6.05$ and $8.28\,\text{nm}^{-3}$. Evidently the same argument cannot be applied to the pre-exponential factor for k_{GG}. Here we observe a decrease in the pre-exponential of an Arrhenius fit to the k_{GG} data from 820 ± 50 to $641 \pm 30\,\text{ns}^{-1}$ as the density is increased from $\rho = 6.05$ and $8.28\,\text{nm}^{-3}$. In this case, increased collisions are likely to result in more

molecules being activated, but once activated they are also more likely to lose energy while in the fleeting *trans* state. Unable to escape the *trans* well, they settle into this state and thus fail to completely traverse the two $G-T$ energy barriers required for a double well hop. A simple analogy is useful here. Imagine a boulder traversing a deep valley (*T* well) between two hills of equal height (i.e. high potential energy). If the boulder has sufficient kinetic energy to cross the first hill (i.e. high temperature), it will also cross the second hill provided it does not lose energy on the way through collisions with other boulders (i.e. provided density is sufficiently low). If it loses sufficient kinetic energy (e.g. by collisions at high density), it will not escape the deep valley. The pre-exponential factors are also much lower than those for k_{GT}. For both densities, the slopes of the Arrhenius plots in Figure 3 are significantly steeper for k_{GG} than for k_{GT}, (assuming Arrhenius behaviour, at $\rho = 6.05\,\mathrm{nm}^{-3}$ $E_a = 10.8 \pm 0.1$ and $8.4 \pm 0.1\,\mathrm{kJ\,mol}^{-1}$ for k_{GG} and k_{GT} respectively). This is consistent with the notion that the molecules need to be activated to a higher energy in order to undergo a double well jump. Since the pre-exponential factor cannot be directly related to the collision frequency, the double jump process can be considered non-Arrhenius.

The results from the bulk fluid calculations confirm that the double jump process is indeed an important one, especially at high temperatures and low densities where it is likely to occur.

We now consider how the kinetics of isomerisation are affected by confinement. As shown previously [6],

confinement under the conditions studied produces layering with high density regions close to the wall, and a region in the centre that approaches a uniform density as the pore width increases. Table 2 shows how k_{GT} and k_{GG} vary as a function of temperature and density for four pore widths ($H = 4\sigma$, 6σ, 8σ and 10σ), with results for k_{TG} given in [6]. As noted in our earlier work, [6] the trends observed for k_{GT} and k_{TG} in the bulk system are also apparent here, although the rate constants are generally smaller. Both k_{GT} and k_{TG} obey an Arrhenius rate law, with slightly reduced activation energies (for the *gauche–trans* transition $E_a = 8.2 \pm 0.2\,\mathrm{kJ\,mol}^{-1}$ for the $H = 4\sigma$ pore at $\rho = 6.05\,\mathrm{nm}^{-3}$, *cf.* $8.4 \pm 1\,\mathrm{kJ\,mol}^{-1}$ in for the bulk system, and for the *trans–gauche* transition $E_a = 11.2 \pm 0.1$ $\mathrm{kJ\,mol}^{-1}$ for the $H = 4\sigma$ pore at $\rho = 6.05\,\mathrm{nm}^{-3}$, *cf.* $11.5 \pm 0.1\,\mathrm{kJ\,mol}^{-1}$ in for the bulk system) but significantly smaller frequency factors in the confined systems (for the *gauche–trans* transition $A = 765 \pm 40\,\mathrm{ns}^{-1}$ for the $H = 4\sigma$ pore at $\rho = 6.05\,\mathrm{nm}^{-3}$, *cf.* $960 \pm 50\,\mathrm{ns}^{-1}$ for the bulk system, and for the *trans–gauche* transition $A = 820 \pm 60\,\mathrm{ns}^{-1}$ for the $H = 4\sigma$ pore at $\rho = 6.05\,\mathrm{nm}^{-3}$, *cf.* $1090 \pm 60\,\mathrm{ns}^{-1}$ in for the bulk system).

The relaxation curves for $R_{G^+,G^+}(t)/\bar{X}_{G^+}$ and $R_{G^+,G^-}(t)/\bar{X}_{G^+}$ were indistinguishable from the bulk data on the scale shown in Figure 2, and the quality of the fits of Equations (12) and (13) to the relaxation curves remained high, and similar to that in the bulk system. Therefore it can be assumed that mechanism (1) also describes the process well in the confined systems.

Table 2.   The rate constants k_{GT}, k_{GG} for butane confined in a Powles slit pore with a surface density of $3.25\,\mathrm{nm}^{-2}$ at the various number densities (ρ), temperatures (*T*) and pore widths.

	k_{GT} (ns^{-1})				k_{GG} (ns^{-1})			
T/K	$H = 4\sigma$	$H = 6\sigma$	$H = 8\sigma$	$H = 10\sigma$	$H = 4\sigma$	$H = 6\sigma$	$H = 8\sigma$	$H = 10\sigma$
Fluid density $\rho = 6.05\,nm^{-3}$, wall surface density $\rho_s = 3.25\,nm^{-2}$								
150	1.18(1)	1.19(2)	1.20(1)	1.26(1)	0.17(3)	0.25(4)	0.18(2)	0.17(2)
200	5.39(4)	6.01(4)	6.08(3)	6.29(3)	1.27(4)	1.21(7)	1.22(4)	1.29(5)
291.6	26.2(2)	27.49(8)	28.4(1)	28.3(3)	8.0(1)	8.90(9)	8.7(1)	9.3(2)
400	66.4(4)	70.2(2)	72.7(2)	73.5(3)	31.1(5)	32.5(6)	32.3(5)	32.7(6)
500	112.0(5)	122.0(3)	128.4(3)	137.0(4)	67(2)	67(1)	66(1)	63.9(7)
Fluid density $\rho = 7\,nm^{-3}$, wall surface density $\rho_s = 3.25\,nm^{-2}$								
150	1.17(2)	1.30(2)	1.33(1)	1.39(1)	0.19(2)	0.19(3)	0.18(1)	0.16(2)
200	6.37(4)	6.96(4)	7.15(4)	7.38(8)	1.26(7)	1.23(6)	1.25(9)	1.17(8)
291.6	30.0(1)	32.5(2)	33.9(2)	34.7(1)	9.3(2)	9.3(1)	9.2(2)	9.4(2)
400	78.8(3)	84.0(2)	88.4(2)	89.5(2)	32.1(4)	33.0(5)	32.3(4)	33.3(5)
500	134.4(5)	145.8(3)	156.4(3)	160.8(4)	68(1)	69(1)	65.7(8)	66.2(8)
Fluid density $\rho = 8.28\,nm^{-3}$, wall surface density $\rho_s = 3.25\,nm^{-2}$								
150	1.32(1)	1.457(7)	1.40(1)	1.50(1)	0.13(3)	0.13(2)	0.10(1)	0.11(3)
200	7.31(4)	8.04(4)	8.17(4)	8.36(5)	1.15(5)	1.07(5)	1.01(4)	0.95(5)
291.6	34.6(2)	38.05(9)	39.9(2)	41.1(1)	9.2(2)	8.7(1)	8.4(1)	8.0(1)
400	88.7(3)	98.6(2)	104.9(3)	108.7(2)	33.5(5)	32.5(5)	30.7(4)	29.6(3)
500	153.2(3)	171.7(4)	183.2(5)	192.7(5)	70(1)	66.3(9)	63.3(8)	59.4(6)

The numbers in parentheses give the standard error in the last figure.

Comparison of the data in Tables 1 and 2 show that at the lower density k_{GG} is generally similar to the bulk value (e.g. at 150K for $\rho = 6.05\,\mathrm{nm}^{-3}$, $k_{GG} = 0.15 \pm 0.02\,\mathrm{ns}^{-1}$ in the bulk and $0.17 \pm 0.3\,\mathrm{ns}^{-1}$ in the $H = 4\sigma$ slit pore) and there is no general trend with an increase in pore width. At higher densities k_{GG} is consistently higher in the confined system (e.g. for $\rho = 8.28\,\mathrm{nm}^{-3}$, $k_{GG} = 0.04 \pm 0.01\,\mathrm{ns}^{-1}$ in the bulk and $0.13 \pm 0.3\,\mathrm{ns}^{-1}$ in the $H = 4\sigma$ slit pore), and decreases towards the bulk value ($k_{GG} = 0.04 \pm 0.01\,\mathrm{ns}^{-1}$) as the pore width increases. This can be seen in Figure 4(a), which shows the variation of k_{GG} with fluid density for the bulk system at 291.6 K, and at a number of pore widths. Similar graphs are obtained at the other temperatures. A result for a pore width of $H = 30\sigma$ is also shown in Figure 4(a), demonstrating that while convergence to the bulk behaviour is occurring, the presence of the wall still affects k_{GG} in these relatively large pores at high fluid density.

The value of k_{GG} increases exponentially with the inverse temperature, as it does in the bulk, however its density dependence is different under confinement. As shown in Figure 4(a), in general k_{GG} falls with an increase in density. However, it is not as dramatic as in the bulk systems, especially at low pore widths. Clearly, the $H = 4\sigma$ data continues to assume values similar to those in the bulk system at $6.05 - 7\,\mathrm{nm}^{-3}$ over the range of densities considered ($6.05 - 9.28\,\mathrm{nm}^{-3}$).

One factor that may contribute to the apparent difference in the density dependence of the confined systems from that of the bulk systems is that the walls are flexible and porous. One would therefore expect an impact due to the fact that the volume available to the fluid is not exactly that used in the calculation of its density according to our definition. Furthermore, there is no 'proper' definition of the volume available to the fluid in this case and there might be a reduction in the 'real' density from the one that was specified. Examination of the density profiles shows that in the higher density fluids, in particular, this does play a role since the density at the centre of the wider pores is reduced from the nominal value, and the density at the position we propose to be the walls (i.e. the boundaries of the central region of width $W = H - \sigma$) is non-zero (see Figure 5). The average density, obtained from integration of the density profile over central region of $W = 3\sigma$ for the $H = 4\sigma$ pore with a nominal fluid density of $8.25\,\mathrm{nm}^{-3}$ is found to be $7.33\,\mathrm{nm}^{-3}$. We note that this is simply another estimate of the average density, and there is no correct average. However, as this gave the average over the region where a large proportion of the molecules lie, it is expected to be more representative than the nominal density defined previously. Therefore, the fluid density was re-estimated using the calculated density profiles in the region, W, and the data for the density dependence of k_{GG} is replotted in Figure 4(b). It can be seen that using
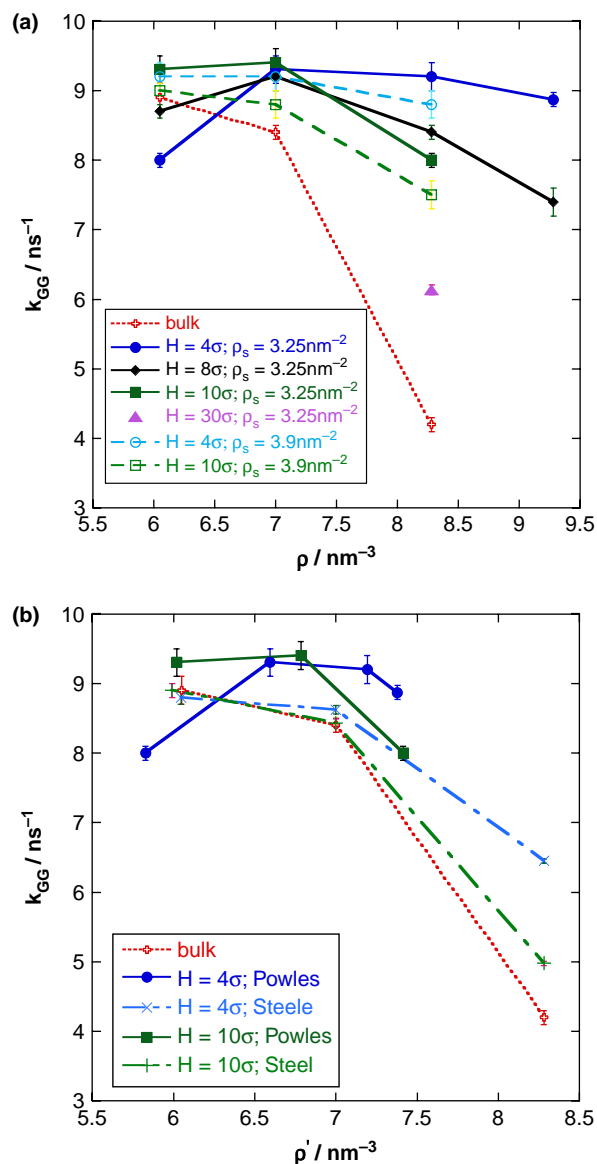

Figure 4. Variation of the value of the rate constant k_{GG} for bulk *n*-butane, and *n*-butane confined in pores of between $H = 4\sigma$ and 30σ in width. In all cases, the temperature is 291.6 K. The lines are added as a guide to the eye. In (a) the results obtained with the Powles slit pore model using two surface densities and various pore widths are compared for a range of nominal fluid densities. They are also compared with the results obtained for a bulk fluid. In (b) the density of the fluid is re-estimated by averaging the fluid density over the width of the pore, W, giving ρ'. Results for the Powles wall model and the Steele wall model are shown for with a surface density of $3.25\,\mathrm{nm}^{-2}$. The error bars are the standard errors.

this estimate of the density, the wider pore now has a qualitative behaviour that is more like that of the bulk system.

We also carried out calculations with a higher wall surface density of $3.9\,\mathrm{nm}^{-2}$ to see if a greater reduction
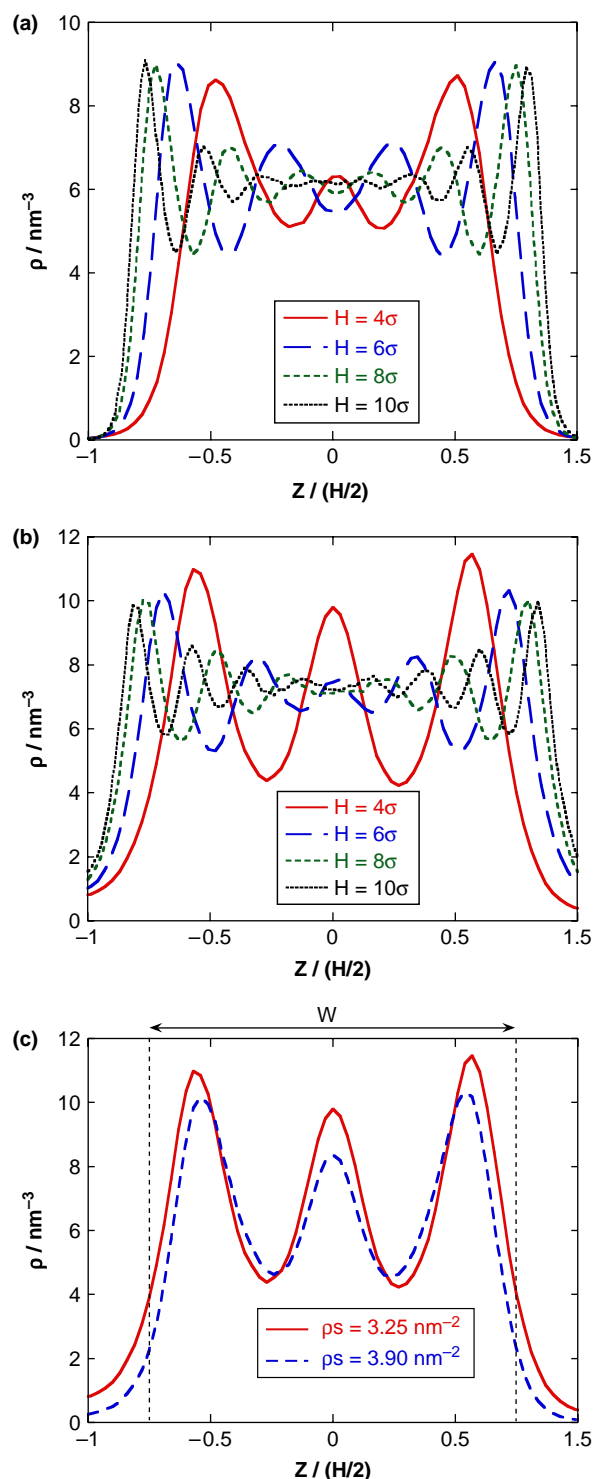
(a)

(b)

(c)

Figure 5.   Density profiles for confined systems with various pore widths. The distance from the centre of the pore, Z, is scaled by $H/2$ in each case. In (a) and (b) the surface density is $3.25\,nm^{-2}$ and the nominal fluid density is (a) $6.05\,nm^{-3}$ and (b) $8.28\,nm^{-3}$. In (c) the results with nominal fluid density of $8.28\,nm^{-3}$ and a pore width of 4σ are given for two wall surface densities: $3.25\,nm^{-2}$ (full line) and $3.9\,nm^{-2}$ (dashed line). The dotted lines mark W, the width of the pore used in the density calculations.

in k_{GG} at higher densities could be observed when the wall becomes less porous. As well as reducing the density at the walls and increasing it slightly in the centre of the pore, this resulted in enhancing the fluctuations in the density profile, as shown for a pore width of 4σ in Figure 5(c). It also resulted in a more significant reduction in k_{GG} with density (see Figure 4(a)), but at this surface density it is clearly not sufficient to fully account for the difference between the bulk and confined results.

An Arrhenius plot comparing the behaviour of k_{GG} in the bulk and confined systems and at different densities and pore widths is given in Figure 6. Clearly, under all conditions there is a linear relationship between $\ln k$ and $1/T$. Table 4 gives the values of the exponential of the intercept and the slope multiplied by $-R$, which would correspond to A and E_a, respectively, should the process be Arrhenius. The value of E_a for the *gauche–gauche* double jump is similar for all the confined and bulk results at the lower densities, and is slightly reduced by confinement in the higher density case although, as discussed previously, this result might simply be due to the difficulties in specifying a density in confined systems. In contrast, the confined and bulk values of the pre-exponential factor show marked qualitative and quantitative differences: decreasing with an increase in density in the bulk systems, but generally increasing with an increase in density in the confined systems.

In order to further examine the effects of the wall model on our results we carried out simulations with a Steele 10-4-3 slit pore. Figure 7(a) shows the density profile for walls with a surface density of $3.25\,nm^{-2}$, matching that of the lower density wall considered with the Powles slit pore, and Figure 7(b) shows the density profile for walls with a much higher surface density that matches that of graphite. Figure 7(c) compares the density profile obtained for the Steele slit pore with that obtained for the Powles slit pore.

The density profiles for the Steele slit pores with a surface density of $3.25\,nm^{-3}$, are similar those for the Powles slit pores, except that the first peak is considerably more pronounced in agreement with earlier studies on simple fluids in slit pores (see, for example [22]), and in addition shoulders are observed within the dense peaks close to the walls, indicating ordering of the butane molecules within these peaks where they are observed to preferentially lie flat against the wall. Butane molecules are able to locate closer to the walls in the Powles slit pore, however the positions of peak maxima are very close and the number of molecules in each layer is similar.

For low fluid densities, the fractions of *trans* conformers in the Powles and Steele slit pores were similar to those in the bulk phase. The exception to this was the smaller pore width of $H = 4\sigma$ for the Steele slit
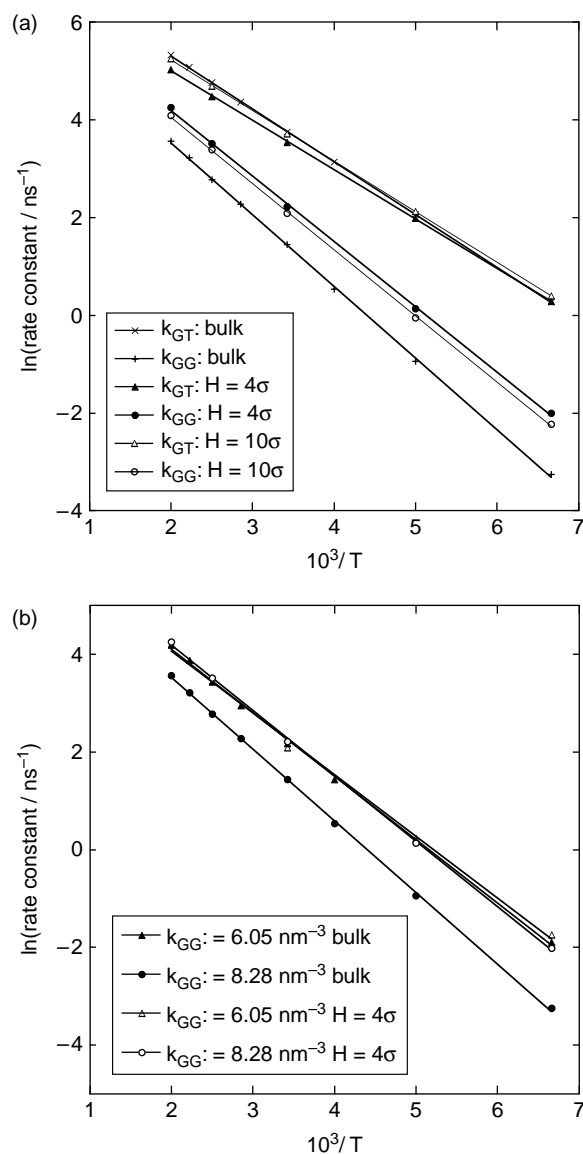
Figure 6. (a) Arrhenius plots of the k_{GT} (triangles) and k_{GG} (circles) at a fluid density $\rho = 8.28\,\text{nm}^{-3}$ and surface density $\rho_\sigma = 3.25\,\text{nm}^{-2}$ in Powles slit pores systems with $H = 4\sigma$ (filled symbols) and 10σ (open symbols). The corresponding bulk data is also shown as crosses: k_{GT} ($\times$) and k_{GG} ($+$). (b) Arrhenius plots of k_{GG} at a fluid densities of $\rho = 6.05\,\text{nm}^{-3}$ (triangles) and $\rho = 8.28\,\text{nm}^{-3}$ (circles) in a bulk system (filled systems) and in Powles slit pores systems with $H = 4\sigma$ (open symbols).

pores (in particular with the graphene surface density) where there was a significant shift in the equilibrium towards the *trans* conformer. As discussed above, at higher fluid densities the Powles modelled wall showed a distinct shift towards *trans*. In contrast the fluid within the Steele slit pores showed negligible shift when the surface density was $3.25\,\text{nm}^{-2}$ and only a very small shift when a graphene surface density was used.
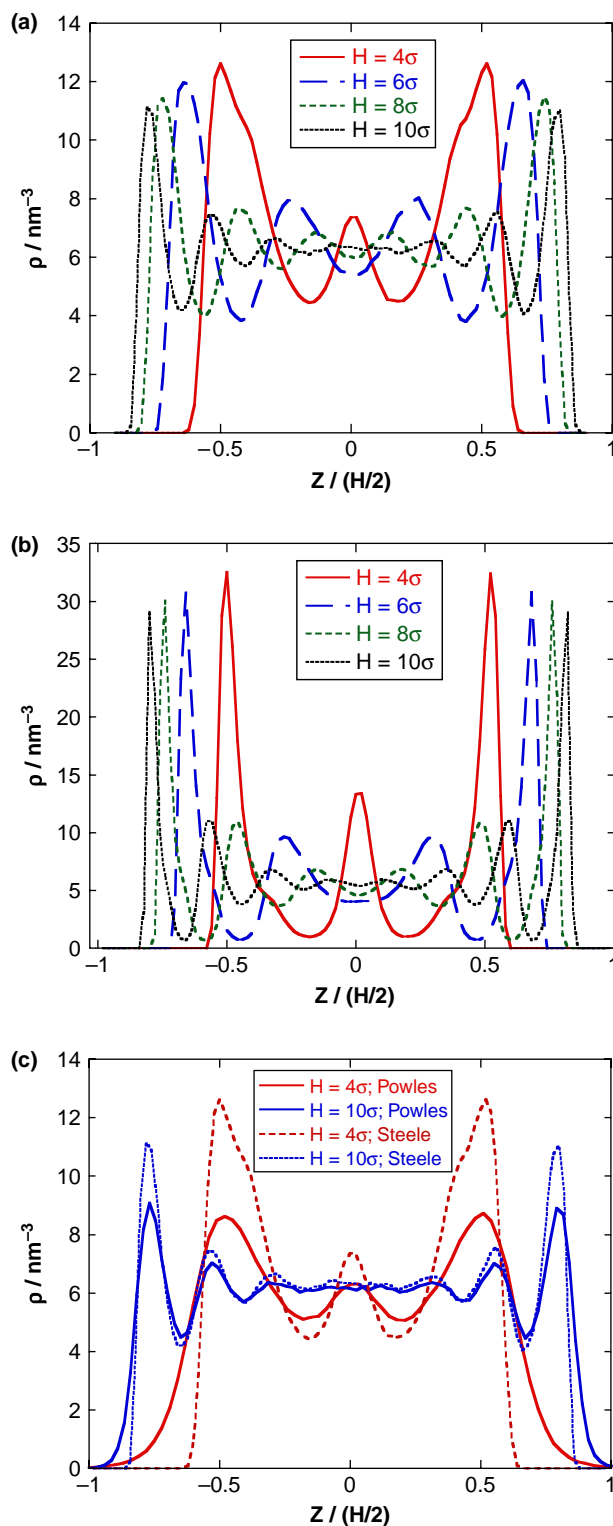

Figure 7. Density profiles obtained using the Steele 10-4-3 potential to model the walls. The temperature was 291.6 K and the fluid density $6.05\,\text{nm}^{-3}$. In (a) the surface density is $3.25\,\text{nm}^{-2}$, which is the same as that used with the Powles wall model in Figure 5(a). In (b) the surface density corresponds to that of graphite. (c) compares the density profiles obtained with the Steele and Powles model.

Table 3 shows the rate constants for the fluid confined by the Steele slit pore and in Figure 4(b) their density dependence is compared with the results obtained in the Powles slit pore. For the lower density fluids, the Powles and Steele slit pores produce similar results, and also good agreement with the bulk rate constants. Generally, k_{GG} is lower in the Steele slit pore than the corresponding Powles slit pore especially at the higher densities (e.g. for $T = 291.6\,\text{K}$, $\rho = 7.0\,\text{nm}^{-3}$ and $H = 4\sigma$, $k_{GG} = 8.6 \pm 0.2\,\text{ns}^{-1}$ for the Steele slit pore and $k_{GG} = 9.3 \pm 0.2\,\text{ns}^{-1}$ for the Powles slit pore; and for $T = 291.6\,\text{K}$, $\rho = 8.28\,\text{nm}^{-3}$ and $H = 4\sigma$, $k_{GG} = 6.3 \pm 0.1\,\text{ns}^{-1}$ for the Steele slit pore and $k_{GG} = 9.2 \pm 0.2\,\text{ns}^{-1}$ for the Powles slit pore), indicating that under these conditions the structure of the walls: their porosity and flexibility are important. The effect upon the rate constants of raising the Steele potential surface density to the value appropriate to graphite can be seen from the values collected in Table 3. The trends with temperature and fluid density are qualitatively similar to those observed when the surface density of the Powles model was raised (although this increase in surface density is much greater and therefore the changes are greater), generally resulting in an increase in k_{GT} and a decrease in k_{TG} and k_{GG}. The preference for molecules to lie flat against the wall is enhanced at this density, and Figure 8 shows a snapshot of the configuration of the molecules for a Steele slit pore with a graphitic surface density and $H = 4\sigma$.

As discussed previously, for fluids in the Powles slit pore, the strong adsorption of the butane and the porosity of the walls make determination of an average density difficult and this contributes to the observed difference in the density dependence of the bulk and confined systems.

However in the systems where the wall is modelled by the Steele potential (and these issues do not arise), we still observe a different behaviour in the confined and bulk systems. This is most pronounced at high densities where the value of k_{GG} is higher in the confined systems and converges towards the bulk value as the pore becomes wider. One may conclude that the walls are likely to play a crucial role in collisional activation/deactivation of the molecules that are instantaneously in the *trans* well on route to the opposite *gauche* well.

Since there are large fluctuations in the density, position dependence in the value of k_{GG} might be anticipated. Correlation of the position of a molecule within the pore and the occurrence of a $G^{\pm}$ to $G^{\mp}$ transition of a molecule was examined, however no clear correlation was observed. In order to examine this more carefully we calculated a local or position dependent relaxation function, defined by Equation (14), and thence a local rate constant. As shown in Figure 9, in the 291.6 K simulation of a fluid confined in the 4σ pore at a density of $8.28\,\text{nm}^{-3}$, there is a small but significant decrease in k_{GG} near the walls. However, this is the low-density region where an increase in k_{GG} would be expected if it is a local effect, and therefore does not explain why the kinetics is faster in the confined systems. These results are consistent with the fact that the relaxation occurs over periods greater than the time for a typical molecule to traverse the pore. This is likely to be more relevant in faster processes.

6.   Conclusions

This work considered the kinetics of isomerisation of n-butane, and how confinement affects the results.

Table 3.   The rate constants k_{GT}, k_{GG} for butane confined by Steele 10-4-3 walls at the various number densities (ρ), wall surface densities (ρ_s) and pore widths.

Rate constant	Graphene, $\rho_\sigma = 38.2\,\text{nm}^{-2}$				Surface density, $\rho_\sigma = 3.25\,\text{nm}^{-2}$			
	$H = 4\sigma$	$H = 6\sigma$	$H = 8\sigma$	$H = 10\sigma$	$H = 4\sigma$	$H = 6\sigma$	$H = 8\sigma$	$H = 10\sigma$
Fluid density $\rho = 6.05\,nm^{-3}$ $T = 291.6\,K$								
k_{GT} (ns^{-1})	31.84(9)	29.31(9)	29.2(1)	29.68(9)	28.27(8)	28.76(8)	29.2(1)	29.22(7)
k_{TG} (ns^{-1})	7.93(8)	9.08(9)	9.1(1)	9.2(1)	8.63(8)	9.26(9)	9.3(1)	9.32(7)
k_{GG} (ns^{-1})	8.8(2)	8.3(1)	8.4(1)	8.3(1)	8.8(1)	8.7(1)	8.8(1)	8.9(1)
Fluid density $\rho = 7\,nm^{-3}$ $T = 291.6\,K$								
k_{GT} (ns^{-1})	38.8(1)	37.3(1)	36.9(1)	36.4(1)	34.6(1)	35.6(1)	35.6(1)	36.2(1)
k_{TG} (ns^{-1})	9.7(1)	12.0(1)	12.3(1)	12.2(1)	10.9(1)	12.1(1)	12.2(1)	12.4(1)
k_{GG} (ns^{-1})	8.5(2)	8.0(2)	8.1(1)	8.4(2)	8.6(2)	8.5(1)	8.5(2)	8.5(2)
Fluid density $\rho = 8.28\,nm^{-3}$ $T = 291.6\,K$								
k_{GT} (ns^{-1})	39.3(1)	41.3(1)	41.5(1)	41.9(1)	38.26(8)	41.8(1)	41.9(1)	42.2(1)
k_{TG} (ns^{-1})	15.3(1)	15.9(1)	16.5(1)	17.0(2)	15.67(7)	16.4(1)	16.9(1)	17.2(1)
k_{GG} (ns^{-1})	5.09(9)	4.7(1)	4.7(1)	4.4(1)	6.3(1)	5.5(1)	5.4(1)	5.0(1)

The fluid temperature was $T = 291.6\,\text{K}$ in all cases. The numbers in parentheses give the standard error in the last figure.
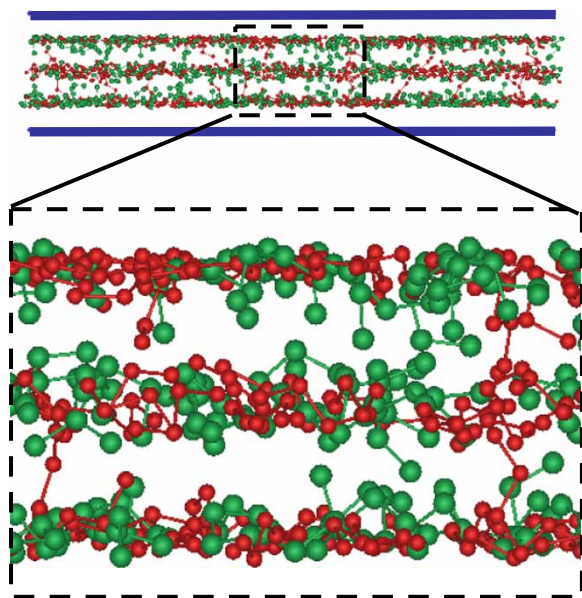
Figure 8. The upper part of the image shows a snapshot of the unit cell from a simulation of butane confined in a Steele slit pore (represented by blue solid lines) with a graphitic surface density. The pore width is $H = 4\sigma$, the fluid density is $8.28\,\mathrm{nm}^{-3}$ and the simulation temperature was 291.6 K. The lower image in the large dashed box is a magnification of the region in the small dashed box. The red molecules are in *trans* conformations and the green molecules are *gauche* conformers. The united atoms of the *trans* conforms are smaller for clarity. The molecules close to the wall show a tendency to lie flat against it.
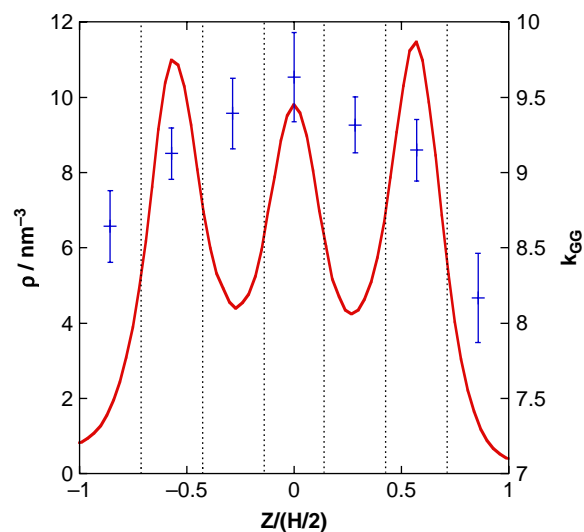

Figure 9. Kinetics and density as a function of position for an $H = 4\sigma$ pore with density $8.28\,\mathrm{nm}^{-3}$ and $T = 291.6$ K. A set of runs with a similar number of particles diffused into the membrane walls were considered to improve numerical accuracy. The red line is the density profile for this set and the crosses show the value of k_{GG} averaged over the regions identified with the dashed lines.

The rate constant k_{GG} was characterised in the bulk fluid, and the G–G transition was found to be due to 'double jumps' across the *trans* minimum. The rate constant decreased with density in the bulk fluid, due to the higher chance of collisions that would allow it to relax into the *trans* state.

We found that under the conditions studied, the confinement influenced the kinetics of isomerisation through details of the interactions with the wall, causing layering and fluctuations in the density profile. When the walls were porous, penetration of fluid atoms into the ill-defined walls also led to changes in the density dependence of the kinetics. For our systems the degree of layering is largely caused by the surface density of the walls, however, the less porous walls produce a greater layering effect, and changes in the rate constant with pore width are generally found to be more significant. Although confinement effects diminish as the pores become wider, they are still significant in the largest pores considered, where $H = 30\sigma$. As shown in our previous work, at high fluid densities confinement results in a decrease in both the activation energy for the T–G barrier and the G–T barrier. This will contribute to the increased value of k_{GG} since the molecules at the same temperature will be more likely to traverse both barriers.

We found only a small variation in the local rate constant with position, which may be explained by the fact that the relaxation process is slow. Recent work has established that in confined hard sphere fluids, the high-density regions also have the largest available volume [30]. If this also applies in our case, it is likely that this would reduce the possibility of collision when the molecule is undergoing a double jump in this region, balancing the effect of increased collisions due to a higher density. It would be of interest to see if a position dependent local rate constant was observed when the relaxation occurred more quickly.

We note that in the case of the very small pores examined, say, in Santiso and Gubbins [31] the flexibility of the walls would become even more significant: in their work they observed severe change in the conformational distribution, with the G configurations no longer giving a local minimum under high confinement. Presumably the more flexible walls would diminish the effects that were observed because the wall molecules would accommodate the forces on the fluid molecules caused by the confinement. In this case, the structure of the walls would play a more significant role. Similarly, in dynamics where strong binding between the wall and fluid molecules occur, details of the wall structure are expected to be more important, and at lower densities it has been shown that details of the fluid wall interactions have a large effect on the self diffusion coefficient, [24] so

Table 4.   Comparison of the Arrhenius parameters for bulk and confined systems.

Porewidth (H)	Trans−gauche		Gauche−trans		Gauche−gauche	
	E_a/kJ mol^{-1}	A/ns^{-1}	E_a/kJ mol^{-1}	A/ns^{-1}	E_a/kJ mol^{-1}	A/ns^{-1}
$\rho = 6.05\,nm^{-3}$						
4σ	11.2(1)	820(60)	8.2(2)	770(40)	10.5(3)	700(100)
6σ	11.29(5)	940(30)	8.20(8)	840(30)	10.0(5)	650(150)
8σ	11.30(8)	980(40)	8.28(9)	890(40)	10.5(2)	750(100)
10σ	11.3(1)	1010(70)	8.23(2)	920(70)	10.6(1)	780(50)
Bulk	11.5(1)	1090(60)	8.4(1)	960(50)	10.8(1)	820(50)
$\rho = 7\,nm^{-3}$						
4σ	11.49(5)	1120(30)	8.42(5)	1000(30)	10.4(2)	800(100)
6σ	11.39(4)	1190(30)	8.36(6)	1060(30)	10.5(3)	800(100)
8σ	11.45(5)	1290(40)	8.44(8)	1140(40)	10.5(2)	800(100)
10σ	11.39(7)	1300(50)	8.4(1)	1150(50)	10.8(2)	800(100)
Bulk	11.78(3)	1670(20)	8.66(6)	1360(40)	10.7(1)	780(40)
$\rho = 8.28\,nm^{-3}$						
4σ	11.31(5)	1240(30)	8.42(5)	1140(30)	11.1(1)	960(60)
6σ	11.37(5)	1430(30)	8.45(6)	1270(40)	11.2(1)	920(70)
8σ	11.46(4)	1600(30)	8.53(5)	1380(40)	11.41(5)	960(30)
10σ	11.52(5)	1700(40)	8.61(6)	1470(50)	11.3(1)	870(40)
Bulk	11.74(2)	2270(20)	9.00(3)	1770(20)	12.2(1)	640(30)

The value of E_a is taken as the slope of a plot of $\ln k$ versus $1/T$, multiplied by $-R$, and the value A is the exponential of the intercept. We note that in the case of the *gauche−gauche* transition it is not appropriate to interpret A as a collision frequency. The fluid temperature was $T = 291.6$ K and the surface density of the walls is $\rho_s = 3.25$ nm^{-2} in all cases.

they are likely to have a more significant effect on other properties of the fluid.

Acknowledgements

Notes

1.   Email: s.brookes@griffith.edu.au
2.   Email: k.travis@sheffield.ac.uk

References

[1]   R. Edberg, D.J. Evans, and G.P. Morriss, *Conformational kinetics in liquid butane by nonequilibrium molecular dynamics*, J. Chem. Phys. 87 (1987), pp. 5700–5708.

[2]   D. Brown and J.H.R. Clarke, *A direct method of studying reaction rates by equilibrium molecular dynamics: application to the kinetics of isomerization in liquid* n-*butane*, J. Chem. Phys. 92 (1990), pp. 3062–3073.

[3]   D. Brown and J.H.R. Clarke, *On the determination of rate constants from equilibrium molecular dynamics simulations*, J. Chem. Phys. 93 (1990), pp. 4117–4122.

[4]   D. Chandler and L.R. Pratt, *Statistical mechanics of chemical equilibria and intramolecular structures of nonrigid molecules in condensed phases*, J. Chem. Phys. 65 (1976), pp. 2925–2940.

[5]   D. Chandler, *Statistical mechanics of isomerization dynamics in liquids and the transition state approximation*, J. Chem. Phys. 68 (1978), pp. 2959–2970.

[6]   K.P. Travis and D.J. Searles, *Effect of solvation and confinement on the trans−gauche isomerization reaction in* n-*butane*, J. Chem. Phys. 125 (2006), 164501.

[7]   E.E. Santiso, M.B. Nardelli, and K.E. Gubbins, *A remarkable shape-catalytic effect of confinement on the rotational isomerization of small hydrocarbons*, J. Chem. Phys. 128 (2008), 034704.

[8]   S. Granick, *Motions and relaxations of confined liquids*, Science 253 (1991), pp. 1374–1379.

[9]   M.A. Castro, S.M. Clarke, A. Inaba, and R.K. Thomas, *Solid monolayers adsorbed at the solid−liquid interfaces studies by incoherent elastic neutron scattering*, J. Phys. Chem. B 101 (1997), pp. 8878–8882.

[10]   J.-C. Wang and K.A. Fichthorn, *Molecular dynamics studies of the effects of chain branching on the properties of confined alkanes*, J. Chem. Phys. 116 (2002), pp. 410–417.

[11]   X. Zhao, S. Kwon, R.D. Vidic, E. Borguet, and J.K. Johnson, *Layering and orientational ordering of propane on graphite: an experimental and simulation study*, J. Chem. Phys. 117 (2002), pp. 7719–7731.

[12]   A.J. Gellman and K.R. Paserba, *Kinetics and mechanism of oligomer desorption from surfaces:* n-*Alkanes on graphite*, J. Phys. Chem. B 106 (2002), pp. 13231–13241.

[13]   M. Heuberger and M. Zäch, *Nanofluidics: structural forces, density anomalies, and the pivotal role of nanoparticles*, Langmuir 19 (2003), pp. 1943–1947.

[14]   M.L. Greenfield and H. Ohtani, *Packing of simulated friction modifier additives under confinement*, Langmuir 21 (2005), pp. 7568–7578.

[15]   C. Alba-Simionesco, B. Coasne, G. Dosseh, G. Dudziak, K.E. Gubbins, R. Radhakrishnan, and M. Sliwinska-Bartkoviak, *Effects of confinement on freezing and melting*, J. Phys. Condens. Matter 18 (2006), pp. R15–R68.

[16]   J.P. Rabe and S. Buchholz, *Direct observation of molecular structure and dynamics at the interface between a solid wall and an organic solution by scanning tunneling microscopy*, Phys. Rev. Lett. 66 (1991), pp. 2096–2099.

[17]   G.C. McGonigal, R.H. Bernhardt, Y.H. Yeo, and D.J. Thomson, *Observation of highly ordered, 2-dimensional* n-*alkane and* n-*alkanol structures on graphite*, J. Vac. Sci. Technol., B 9 (1991), pp. 1107–1110.

[18] T. Müller, T.L. Werblowsky, G.M. Florio, B.J. Berne, and G.W. Flynn, *Ultra-high vacuum scanning tunneling microscopy and theoretical studies of 1-halohexane monolayers on graphite*, Proc. Natl. Acad. Sci. 102 (2005), pp. 5313–5322.

[19] S.T. Cui, P.T. Cummings, and H.D. Cochran, *Molecular simulation of the transition from liquid-like to solid-like behavior in complex fluids confined to nanoscale gaps*, J. Chem. Phys. 114 (2001), pp. 7189–7195.

[20] S. Patil, G. Matei, A. Oral, and P.M. Hoffmann, *Solid or liquid? Solidification of a nanoconfined liquid under nonequilibrium conditions*, Langmuir 22 (2006), pp. 6485–6488.

[21] K. Malek and M.-O. Coppens, *Effects of surface roughness on self- and transport diffusion in porous media in the Knudsen regime*, Phys. Rev. Lett. 87 (2001), 125505.

[22] V.P. Sokhan, D. Nicholson, and N. Quirke, *Fluid flow in nanopores: an examination of hydrodynamic boundary conditions*, J. Chem. Phys. 115 (2001), pp. 3878–3887.

[23] V.P. Sokhan, D. Nicholson, and N. Quirke, *Transport properties of nitrogen in single walled carbon nanotubes*, J. Chem. Phys. 120 (2004), p. 3855.

[24] R.F. Cracknell, D. Nicholson, and K.E. Gubbins, *Molecular dynamics study of the self-diffusion of supercritical methane in slit-shaped graphitic micropores*, J. Chem. Soc., Faraday Trans. 91 (1995), pp. 1377–1383.

[25] J. Jacobsen, K.W. Jacobsen, and J.P. Sethna, *Rate theory for correlated processes: double jumps in adatom diffusion*, Phys. Rev. Lett. 79 (1997), pp. 2843–2846.

[26] H.S. Chan and K.A. Dill, *Protein folding in the landscape perspective: Chevron plots of non-Arrhenius kinetics*, Proteins: Struct., Funct., Genet. 30 (1998), pp. 2–33.

[27] J.-P. Ryckaert and A. Bellemans, *Molecular dynamics of liquid alkanes*, Discuss. Faraday Soc. 66 (1978), pp. 95–106.

[28] J.G. Powles, S. Murad, and P.V. Ravi, *A new model for permeable micropores*, Chem. Phys. Lett. 188 (1992), pp. 21–24.

[29] W.A. Steele, *The Interaction of Gases with Solid Surfaces*, Pergamon, Oxford, 1974.

[30] J. Mittal, T.M. Truskett, J.R. Errington, and G. Hummer, *Layering and position-dependent diffusive dynamcis of confined fluids*, Phys. Rev. Lett. 100 (2008), 145901.

[31] E.E. Santiso and K.E. Gubbins, *Multi-scale molecular modeling of chemical reactivity*, Mol. Simul. 30 (2004), pp. 679–748.